Numerical simulation of premixed combustion using an enriched finite element method

Fedderik van der Bos *, Volker Gravemeier

Emmy Noether Research Group "Computational Multiscale Methods for Turbulent Combustion", Technische Universität München, Boltzmannstrasse 15, D-85747 Garching, Germany
Institute for Computational Mechanics, Technische Universität München, Boltzmannstrasse 15, D-85747 Garching, Germany

A R T I C L E   I N F O

A B S T R A C T

In this paper we present a novel discretization technique for the simulation of premixed combustion based on a locally enriched finite element method (FEM). Use is made of the *G*-function approach to premixed combustion in which the domain is divided into two parts, one part containing the burned and another containing the unburned gases. A level-set or *G*-function is used to define the flame interface separating burned from unburned gases. The eXtended finite element method (X-FEM) is employed, which allows for velocity and pressure fields that are discontinuous across the flame interface. Lagrange multipliers are used to enforce the correct essential interface conditions in the form of jump conditions across the embedded flame interface. A persisting problem with the use of Lagrange multipliers in X-FEM has been the discretization of the Lagrange multipliers. In this paper the distributed Lagrange multiplier technique is adopted. We will provide results from a spatial convergence analysis showing good convergence. However, a small modification of the interface is required to ensure a unique solution. Finally, results are presented from the application of the method to the problems of moving flame fronts, the Darrieus–Landau instability and a piloted Bunsen burner flame.

© 2009 Elsevier Inc. All rights reserved.

1. Introduction

In this paper we present a discretization technique for the simulation of premixed combustion based on a locally enriched finite element method (FEM). In many premixed flames of interest, the typical chemical length scale ℓ_f is small compared to the smallest turbulent length scale η [1]. The flame may be represented as an infinitely small interface I_f separating burned from unburned gases. This approach has the advantage that it is not required to compute additional evolution equations for all species involved in a combustion process as well as the chemical reactions schemes. Instead, the chemistry is modeled in terms of a flame speed and the discontinuities that are imposed on the velocity and pressure in terms of jump conditions across the interface [1,2]. In literature this approach is often referred to as the *G*-function approach to premixed turbulent combustion [1,3] due to the level-set function *G* used to track the interface (see Fig. 1).

From a computational point of view two aspects of the *G*-function approach to premixed turbulent combustion are particulary challenging. This is, first of all, the need to accurately track and capture the flame interface and, second, the need to represent the discontinuities encountered across the flame interface. FEM as adopted in this paper allow for an accurate capturing of the flame topology. Within a FEM, the *G*-function is continuously defined across the complete domain,

---

* Corresponding author. Address: Emmy Noether Research Group "Computational Multiscale Methods for Turbulent Combustion", Technische Universität München, Boltzmannstrasse 15, D-85747 Garching, Germany. Tel.: +49 89 28915253.
E-mail addresses: bos@lnm.mw.tum.de (F. van der Bos), vgravem@lnm.mw.tum.de (V. Gravemeier).
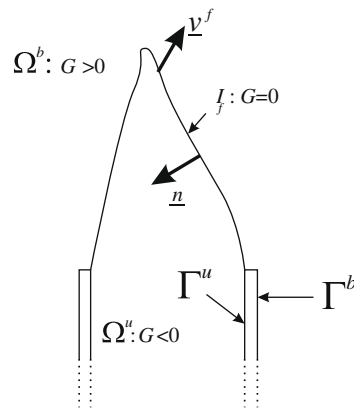
Fig. 1. Graphical interpretation of the domain Ω as set by the G-function. The flame corresponds to those points for which $G = 0$. By definition the normal **n** is pointing into the unburned domain Ω^u.

whereas other methods, such as the volume-of-fluids method, generally require interpolation between grid points. Standard FEM, however, do not allow for discontinuous solutions. Therefore, in this paper, the finite element space is locally enriched near the interface with shape functions that are discontinuous across the flame interface to allow for discontinuous solutions.

Locally enriched FEM have been proposed by various authors and adopted for various applications. Belytschko et al. [4–6], Moes et al. [7], Comi et al. [8,9] as well as Mariani and Perego [10] used such a method to model crack-problems and referred to the method as the eXtended FEM (X-FEM). Other successful applications of the X-FEM for two-phase flow can be found in articles by Chessa and Belytschko [11], Minev et al. [12] and Groß et al. [13–15] and for fluid-structure interaction by Gerstenberger and Wall [16,17], Fries and Belytschko [18], Kölke-Zilian and Legay [19–21]. Another contribution where a locally enriched FEM is used to simulate thermal oxidation in electronical devices can be found in Rao et al. [22].

The G-function approach to premixed turbulent combustion was originally proposed by Williams [3] and is extensively discussed in [1]. As already mentioned, it involves two important ingredients which should account for the chemistry. This is, first of all, the definition of the relative flame speed **s**, which is the speed with which the flame interface is moving relative to the local flow-field, and, second, the jump conditions that are imposed on the velocity and pressure fields to model gas expansion [2,23–25]. Here we will only consider definitions that hold for the corrugated-flame regime when $\ell_f / \eta \ll 1$. However, modifications as proposed by, e.g. Class and Matalon [2,25] that should hold in the thin-reaction-zones regime when $\ell_f / \eta \sim 1$ can in principle also be used. Earlier examples where the G-function approach is used to numerically simulate premixed turbulent combustion can be found in papers by Nguyen et al. [26], Gibou et al. [27], Rastigejev and Matalon [28], Pitsch and Duchamp de Lageneste [29,30], Kim and Menon [31], and Law and co-workers [32–35].

Due to the essential boundary conditions encountered over the flame interface, the problem type studied here differs considerably from the problem types for which X-FEM have already been developed, e.g. two-phase flow problems [11–15]. Some of the new contributions presented in this paper are directly related to the way these boundary conditions are enforced. For a number of reasons given below, we have chosen to use the distributed Lagrange multiplier (DLM) technique for the discretization of the Lagrange multipliers as recently proposed by Kölke-Zilian and Legay [21,20].

Traditional approaches for discretizing the Lagrange multipliers rely on shape functions constructed over the interface, see, e.g. [7,36,37]. For two-dimensional problems, in which the interface is a line, this is not a problematic issue. However, applying such methods to three-dimensional problems poses a number of challenges. In particular the requirement to construct a two-dimensional coordinate system related to the interface is challenging, certainly considering the very irregular shape a turbulent flame may attain, see, e.g. Pitsch [30]. The DLM technique does not require the construction of an interface-related coordinate system. Hence, the DLM technique is considerably more convenient than traditional approaches from an implementation point of view.

Although we only deal with two-dimensional problems in this paper, we already adopt the DLM technique, since it is our intention to extend the method to three-dimensional problems soon. As already very briefly discussed in [20,21] there is a need to introduce some form of stabilization to ensure a unique solution. We propose small modifications to the interface in the form of stitches. In Section 3.3.3 we will extensively discuss the DLM technique and results from a spatial convergence analysis are provided in Section 4.2 showing good convergence.

For the stabilization of the level-set function use is made of the recently introduced edge-based stabilization technique [38–40]. This type of stabilization prevents the development of kinks across element edges and the resulting large inter-element discrepancies of the gradient magnitude. This is of particular importance as it assumed that the G-function satisfies the signed-distance property. Consequently, the gradient magnitude $|\nabla G|$ should be uniform, close to unity and does not allow for inter-element discrepancies of the gradient magnitude. Moreover, it will be shown that without this stabilization technique kinks will emerge that, e.g. prevent an accurate prediction of the growth rate of a Darrieus–Landau instability.

The layout of this paper is as follows. First, in Section 2 the governing equations are described. In Section 3 the enriched finite element method is introduced, and further details of the discretization are given. Numerical results are presented in Section 4. Finally, conclusions are drawn in Section 5.

2. Governing equations

2.1. Geometry and notation

As mentioned in the introduction, in the G-function approach we distinguish between two separate flow domains within the domain $\Omega \subset \mathbb{R}^2$: one containing unburned flow gases Ω^u and another containing burned gases Ω^b. These two domains are separated by the flame interface I_f which normal $\mathbf{n}$, by definition, is pointing into the unburned domain (see Fig. 1) [1].

The complete "geometry" of the flow problem is set by the G-function. The unburned flow domain Ω^u corresponds to that part of the domain where $G < 0$, whilst the burned region Ω^b corresponds to $G > 0$. The flame interface I_f consequently corresponds to those points for which $G = 0$. Because of the dependence of the geometry on G, burned and unburned flow domains as well as the flame interface are frequently denoted with G in their argument, i.e., $\Omega^u(G), \Omega^b(G)$ and $I_f(G) = I_f^G$.

Throughout this paper, Einstein notation is adopted, such that summation is implied over repeated indices and vectors can be denoted as u_i. Additionally, for notational convenience, any variable f denoted with a $*$ – superscript simultaneously represents an unburned and a burned realization of this variable. Hence, e.g. $f^* = c$ simultaneously implies $f^u = c$ and $f^b = c$. This notation is also applied to equations as well as functional spaces.

2.2. Navier–Stokes equations

The governing equations in both domains Ω^* are the incompressible Navier–Stokes equations

$$\rho^* \partial_t u_i^* + \rho^* u_j^* \partial_j u_i^* + \partial_i p^* - \mu^* \partial_j \epsilon_{ij}(\mathbf{u}^*) = 0 \quad \text{in } \Omega^*, \tag{1}$$

$$\partial_j u_j^* = 0 \quad \text{in } \Omega^*, \tag{2}$$

$$u_i^* = g_i^* \quad \text{on } \Gamma_D^* = \Gamma_{D_0}^* \cup \Gamma_{D_{LM}}^*, \tag{3}$$

$$\sigma_{ij}^* n_j = h_i^* \quad \text{on } \Gamma_N^*, \tag{4}$$

where $\Gamma_{D_0}^* \cap \Gamma_{D_{LM}}^* = \emptyset$. In (1)–(4) ρ^* denotes the density, u_i^* the i-th Cartesian velocity component, p^* the pressure, μ^* the dynamic viscosity, $\epsilon_{ij}(\mathbf{u}) = (\partial_i u_j + \partial_j u_i)/2$ the rate-of-strain tensor and $\sigma_{ij}^* = -p^* \delta_{ij} + \mu^* \epsilon_{ij}(\mathbf{u}^*)$ the stress tensor, with δ_{ij} denoting the Kronecker delta function.

The boundary of the domain Ω is given by $\partial\Omega = \Gamma^u \cup \Gamma^b$, while the boundaries of the two separate domains containing burned and unburned gases Ω^* are given by $\partial\Omega^* = \Gamma^* \cup I_f$. On Γ_D^* and Γ_N^* Dirichlet and Neumann boundary conditions, respectively, are imposed. We differentiate between two methods that are used to enforce the Dirichlet boundary conditions. On $\Gamma_{D_0}^*$ Dirichlet boundary conditions are enforced in the traditional way which requires the Dirichlet boundary conditions to be fulfilled through the functional (sub)spaces. However, in cases where the support of the locally enriched finite element space $\mathcal{D} \subset \Omega$ may coincide with Γ_D^*, there is a need to enforce the Dirichlet boundary conditions using Lagrange multipliers [41–44]. The use of Lagrange multipliers to enforce the Dirichlet boundary conditions results in additional equations that need to be solved. Therefore we use a mixed approach such that on $\Gamma_{D_0}^*$ the cheaper direct approach can be adopted, whilst on $\Gamma_{D_{LM}}^*$ Lagrange multipliers are used to enforce the Dirichlet boundary conditions.

The boundary conditions over the flame interface $I_f = \partial\Omega^u \cup \partial\Omega^b$ are defined in terms of multiple jump conditions that need to be enforced across the flame interface I_f:

$$[\![\rho(v_n^f - u_n)]\!] = 0, \tag{5}$$

$$[\![u_\tau]\!] = 0, \tag{6}$$

$$[\![\rho(v_n^f - u_n)u_n + p]\!] = 0. \tag{7}$$

Here $u_n = \mathbf{u} \cdot \mathbf{n}$ and $u_\tau = \mathbf{u} \cdot \tau$ are the normal and tangential velocity at the interface, respectively, $[\![f]\!] = f^b - f^u$ is the jump operator over I_f and $\mathbf{v}^f$ represents the flame speed with respect to a fixed frame of reference (see Fig. 1). By enforcing (5)–(7), it is assumed that the flame interface is so thin that in the tangential direction τ no forces are applied nor any mass transferred and both mass and momentum are conserved in the normal direction, neglecting the effect of viscosity.

Next the mass flux is introduced as $M = \rho^*(v_n^f - u_n^*)$, which can be denoted without a superscript, since $\rho^u(v_n^f - u_n^u) = \rho^b(v_n^f - u_n^b)$ due to (5). Inserting the definition of the mass flux into (7) results in the following mixed boundary condition over the interface in the normal direction:

$$[\![Mu_n + p]\!] = 0. \tag{8}$$

Using (5) we may express the jump condition for the normal velocity in terms of the mass flux M

$$[\![u_n]\!] = u_n^b - u_n^u = (v_n^f - u_n^u) - (v_n^f - u_n^b) = \left(\frac{1}{\rho^u} - \frac{1}{\rho^b}\right)M = -M[\![\rho^{-1}]\!] \tag{9}$$

such that the pressure jump is given by

$$[\![p]\!] = -M[\![u_n]\!] = M^2[\![\rho^{-1}]\!]. \tag{10}$$

As will be shown in the next section, this pressure jump condition can be incorporated by rewriting the stress part over the interface that emerges after integration by parts.

The two different boundary conditions across the interface I_f, the mixed boundary condition (8) in the normal and the Dirichlet boundary condition (6) in the tangential direction are both treated as essential boundary conditions. This observation immediately sets the two-phase flow problem considered in this paper apart from multi-phase flow problems that deal with immiscible fluid interfaces. The boundary conditions across the interface for such flows are pure Neumann (natural) boundary conditions relating the stress components on both sides of the interface. Such boundary conditions can be enforced in a straightforward manner. However, essential boundary conditions over an embedded interface cannot be incorporated in such a straightforward manner. This is due to the fact that the traditional way of enforcing Dirichlet boundary conditions, i.e., via functional spaces, is difficult if not impossible to apply. Therefore, Lagrange multipliers will also be used to enforce the jump boundary conditions for the normal (9) and tangential velocity (6) across the interface, see Section 3.3.3.

2.3. Level-set function

In order to define and track the flame interface, use is made of a level-set function G and, at any point in time, the flame interface I_f is given by those points for which $G = 0$. Away from the interface, we assume that the level-set function is defined as a signed-distance function such that

$$|G(x)| = \min_{y \in I_f} |y - x| \tag{11}$$

and $|\nabla G| = \sqrt{(\partial_k G)(\partial_k G)} \approx 1$.

The G-function is advected through the domain Ω with the flame speed $\mathbf{v}^f$ resulting in the following evolution equation:

$$\partial_t G + v_j^f \partial_j G = 0 \quad \text{in } \Omega. \tag{12}$$

Note that the actual definition of the flame speed $\mathbf{v}^f$ is only physically relevant in the vicinity of the interface. Hence, we should formally speak of an *extended* flame speed. We have chosen not to do so, but do want to point out that there is a large amount of freedom to modify the flame speed away from the interface, when necessary.

The actual definition of the flame speed $\mathbf{v}^f$ is based on the relative flame speed $\mathbf{s}^* = \mathbf{v}^f - \mathbf{u}^*$. This is the speed with which the flame is traveling relative to the flow field $\mathbf{u}^*$. Defining the normal and tangential vector at the interface, respectively, as [1]

$$\mathbf{n} = -\frac{\nabla G}{|\nabla G|}, \qquad \tau = [n_2, -n_1], \tag{13}$$

we assume the normal and tangential components of the *unburned* relative flame speed $s_n^u = \mathbf{s}^u \cdot \mathbf{n}$ and $s_\tau^u = \mathbf{s}^u \cdot \tau$ to be given by Peters [1] and Nguyen et al. [26]

$$s_n^u = s_L, \tag{14}$$
$$s_\tau^u = 0, \tag{15}$$

where s_L denotes the laminar flame speed.

In order to arrive at an expression for the flame speed $\mathbf{s}^*$ that is well defined in both the unburned and burned flow-domain and preserves C^0 continuity of the G-function (12) across the interface [32], observe that $\mathbf{s}^*$ should satisfy the following jump condition: $[\![s_i]\!] = -[\![u_i]\!]$. Then $[\![u_i + s_i]\!] = 0$ such that there is a continuous transition for (12) across the interface. One can readily verify that the following definition of the relative flame speed satisfies the required jump condition [1,32]:

$$\mathbf{s}^*(G) = \frac{\rho^u s_n^u}{\rho^*} \mathbf{n}. \tag{16}$$

Using the definition of the relative flame speed $\mathbf{s}^*$ above, we may express the evolution equation of the G-function Eq. (12) as

$$\partial_t G + (u_j^* + s_j^*(G)) \cdot \partial_j G = 0, \quad \forall \mathbf{x} \in \Omega^*. \tag{17}$$

Note that (17) implies two equations, since s^* and u^* are only well defined in Ω^*.

3. Discrete method

In this section the complete discretization will be described. First, in Section 3.1 the weak formulation of the Navier–Stokes equation will be given and the time-stepping scheme is introduced. In Section 3.2 this is repeated for the G-function. In Section 3.3 the discrete solution spaces are given as well as further details regarding stabilization and evaluation of the integrals. The fluid-G-function interaction (FGI) is described in Section 3.4.

3.1. Navier–Stokes equations

In the following, the weak formulation of the Navier–Stokes equations (1)–(4) in combination with the boundary conditions across the interface will be given. Here, we assume G' to be a given realization of the level-set function that separates the space Ω into a burned and an unburned part. We start by introducing the following solution spaces for velocity and pressure, respectively,

$$\mathcal{V}_g^* = \left\{ \mathbf{u} \in [H^1(\Omega^*(G'))]^2 \big| \mathbf{u}|_{\Gamma_{D_0}^*(G')} = \mathbf{g}^* \right\}, \quad \mathcal{Q}^* = L_2(\Omega^*(G')). \tag{18}$$

Next, (1) and (2) are multiplied by test functions $\mathbf{w}^* \in \mathcal{V}_0^*$ and $q^* \in \mathcal{Q}^*$, respectively, and afterwards, integrated over the domains $\Omega^*(G')$ to arrive at the following weighted-residual formulation for the momentum and continuity equations:

$$\int_{\Omega^*(G')} w_i \left(\rho \partial_t u_i + \rho u_j \partial_j u_i + \partial_i p - \mu \partial_j \epsilon_{ij}(\mathbf{u}) \right) dA = 0, \tag{19}$$

$$\int_{\Omega^*(G')} q \left(\partial_j u_j \right) dA = 0. \tag{20}$$

Applying integration by parts to the pressure and viscous terms in (19), yields the following variational formulation of the momentum equation:

$$\int_{\Omega^*(G')} w_i(\rho \partial_t u_i + \rho u_j \partial_j u_i) - (\partial_i w_i)p + \mu\,\epsilon_{ij}(\mathbf{w})\epsilon_{ij}(\mathbf{u})\,dA - \int_{\partial\Omega^*(G')} w_i \sigma_{ij} n_j\,dS = 0, \tag{21}$$

where we have exploited that $(\partial_j w_i)\epsilon_{ij}(\mathbf{u}) = \epsilon_{ij}(\mathbf{w})\epsilon_{ij}(\mathbf{u})$ because of the symmetry of the matrix ϵ_{ij}.

In the following step, the burned and unburned realization of (21) are taken together, and those terms required to enforce the Dirichlet boundary conditions using Lagrange multipliers on $\Gamma_{D_{LM}}$ as well as the boundary conditions across the flame interface $I_f^{G'}$ are included:

$$\int_{\Omega^{G'}} w_i(\rho \partial_t u_i + \rho u_j \partial_j u_i) - (\partial_i w_i)p + \mu\,\epsilon_{ij}(\mathbf{w})\epsilon_{ij}(\mathbf{u})\,dA - \int_{I_f^{G'}} [\![w_i \sigma_{ij}]\!] n_j\,dS + \int_{\Gamma_{D_{LM}}^{G'}} w_n \pi_n + w_\tau \pi_\tau\,dS + \int_{I_f^{G'}} [\![w_n]\!]\lambda_n + [\![w_\tau]\!]\lambda_\tau\,dS$$

$$= \int_{\Gamma_N^{G'}} w_i h_i\,dS, \tag{22}$$

$$\int_{I_f^{G'}} l_n [\![u_n]\!]\,dS = \int_{I_f^{G}} l_n J_n\,dS, \tag{23}$$

$$\int_{I_f^{G'}} l_\tau [\![u_\tau]\!]\,dS = \int_{I_f^{G}} l_\tau J_\tau\,dS, \tag{24}$$

$$\int_{\Gamma_{D_{LM}}^{G'}} m_n u_n\,dS = \int_{\Gamma_{D_{LM}}^{G'}} m_n g_n\,dS, \tag{25}$$

$$\int_{\Gamma_{D_{LM}}^{G'}} m_\tau u_\tau\,dS = \int_{\Gamma_{D_{LM}}^{G'}} m_\tau g_\tau\,dS. \tag{26}$$

In these equations, $J_n = -M[\![\rho^{-1}]\!]$ and $J_\tau = 0$ are the jump conditions in the normal and tangential direction, respectively, $\Omega^{G'} = \Omega^u(G') \cup \Omega^b(G')$ and $\Gamma^{G'} = \Gamma^u(G') \cup \Gamma^b(G')$, while the pairs $(\lambda_n, \lambda_\tau) \in \Lambda_f(G') = [L_2(\Gamma_{I_f^{G'}})]^2$ and $(\pi_n, \pi_\tau) \in \Lambda_{D_{LM}}(G') = \left[L_2\left(\Gamma_{D_{LM}}^{G'} \right) \right]^2$ in (22) are the Lagrange multipliers used to enforce the boundary conditions across the interface and on $\Gamma_{D_{LM}}$, respectively. Obviously, $(l_n, l_\tau) \in \Lambda_f(G') = \left[L_2\left(\Gamma_{I_f^{G'}} \right) \right]^2$ and $(m_n, m_\tau) \in \Lambda_{D_{LM}}(G') = \left[L_2\left(\Gamma_{D_{LM}}^{G'} \right) \right]^2$ are the pairs of test functions related to these Lagrange multipliers.

In the next step we neglect the effect of viscosity at the flame interface I_f and then rewrite the remaining $[\![w_n p]\!]$ term using the identity: $[\![fg]\!] = [\![f]\!]\{\{g\}\} + \{\{f\}\}[\![g]\!]$, where $\{\{f\}\} = (f^b + f^u)/2$ is the average across the flame interface [45]. Applying this identity to (22) and replacing the resulting $[\![p]\!]$ with $M^2[\![\rho^{-1}]\!]$ (see (10)) allows us to incorporate the jump condition for the pressure. Now (22) transforms into

$$\int_{\Omega^{G'}} w_i(\rho \partial_t u_i + \rho u_j \partial_j u_i) - (\partial_i w_i)p + \mu\,\epsilon_{ij}(\mathbf{w})\epsilon_{ij}(\mathbf{u})\,dA + \int_{I_f^{G'}} [\![w_n]\!]\{\{p\}\}\,dS + \int_{\Gamma_{D_{LM}}^{G'}} w_n \pi_n + w_\tau \pi_\tau\,dS$$

$$+ \int_{I_f^{G'}} [\![w_n]\!]\lambda_n + [\![w_\tau]\!]\lambda_\tau\,dS = -\int_{\Gamma_N^{G'}} w_i h_i\,dS - \int_{I_f^{G'}} \{\{w_n\}\} M^2 [\![\rho^{-1}]\!]\,dS. \tag{27}$$

To arrive at a semi-discrete (discrete in time) formulation for these equations, we introduce the implicit backward Euler scheme for time integration. Now the complete system of equations can be put into the following semi-discrete system:

$$B^F(\mathbf{W}, \mathbf{U}^{n+1}; \mathbf{u}^{n+1}, \Delta t | G') = F^F(\mathbf{W}; \mathbf{u}^n, \Delta t | G'). \tag{28}$$

Here $\mathbf{U}^{n+1} = \mathbf{U}(t_{n+1})$, $\mathbf{U} = (\mathbf{u}, p, \lambda_n, \lambda_\tau, \pi_n, \pi_\tau)$, $\mathbf{W} = (\mathbf{w}, q, l_n, l_\tau, m_n, m_\tau)$ and $\Delta t = t_{n+1} - t_n$. The operators B^F and F^F collect the left and right hand side, respectively, of (20) and (23)–(27) and are, respectively, given by

$$B^F(\mathbf{W}, \mathbf{U}; \boldsymbol{\beta}, \Delta t|G) = \int_{\Omega^G} w_i((\Delta t)^{-1}\rho u_i + \rho\beta_j\partial_j u_i) - (\partial_i w_i)p + \mu\,\epsilon_{ij}(\mathbf{w})\epsilon_{ij}(\mathbf{u})\,dA + \int_{\Omega^G} q\,(\partial_j u_j)\,dA + \int_{I_f^G} [\![w_n]\!]\{\{p\}\}\,dS$$

$$+ \int_{I_f^G} [\![w_n]\!]\lambda_n + [\![w_\tau]\!]\lambda_\tau\,dS + \int_{\Gamma_{D_{LM}}^G} w_n\pi_n + w_\tau\pi_\tau\,dS + \int_{I_f^G} l_n[\![u_n]\!] + l_\tau[\![u_\tau]\!]\,dS + \int_{\Gamma_{D_{LM}}^G} m_n u_n + m_\tau u_\tau\,dS \tag{29}$$

and

$$F^F(\mathbf{W}; \mathbf{u}^n, \Delta t|G) = (\Delta t)^{-1}\int_{\Omega^G} w_i\rho u_i^n\,dA - \int_{\Gamma_N^G} w_i h_i\,dS - \int_{I_f^G}\{\{w_n\}\}M^2[\![\rho^{-1}]\!]\,dS - \int_{I_f^G} l_n M[\![\rho^{-1}]\!]\,dS$$

$$+ \int_{\Gamma_{D_{LM}}^G(G)} m_n g_n + m_\tau g_\tau\,dS. \tag{30}$$

An iterative solution technique is used to solve the non-linear system (28). For each iteration $s > 0$, the solution $\mathbf{U}^{n+1,s} \in \left[\mathcal{V}_g^b(G') \cup \mathcal{V}_g^u(G')\right] \times [\mathcal{Q}^b(G') \cup \mathcal{Q}^u(G')] \times \Lambda_f(G') \times \Lambda_{D_{LM}}(G')$ is determined that satisfies

$$B^F(\mathbf{W}, \mathbf{U}^{n+1,s}; \mathbf{u}^{n+1,s-1}, \Delta t|G') = F^F(\mathbf{W}; \mathbf{u}^n, \Delta t|G'), \tag{31}$$

for all $\mathbf{W} \in \left[\mathcal{V}_0^b(G') \cup \mathcal{V}_0^u(G')\right] \times [\mathcal{Q}^b(G') \cup \mathcal{Q}^u(G')] \times \Lambda_f(G') \times \Lambda_{D_{LM}}(G')$. This process is continued until $\mathbf{u}^{n+1,s}$ and $p^{n+1,s}$ are converged based on the norm

$$\|(\mathbf{u}^{n+1,s}, p^{n+1,s}) - (\mathbf{u}^{n+1,s-1}, p^{n+1,s-1})\|^2 = \int_\Omega |\mathbf{u}^{n+1,s} - \mathbf{u}^{n+1,s-1}|^2 + (p^{n+1,s} - p^{n+1,s-1})^2\,dx. \tag{32}$$

3.2. Level-set equation

The semi-discrete formulation of the G-equations (17) follows analogously to that of the fluid part described in the previous subsection. Throughout this subsection, with $(\mathbf{u}')^*$ we denote a given realization of the burned and unburned flow-field, and with G' we denote the realization of the G-function linked to $(\mathbf{u}')^*$. Furthermore, we consider the following functional space with global support for the G-function:

$$\mathcal{R} = \left\{G \in C_0(\Omega)|G|_{\Gamma_{G_0}} = 0\right\}, \tag{33}$$

where Γ_{G_0} corresponds to a set of points that can be used to fix the flame interface.

Eq. (17) are multiplied with test functions $r \in \mathcal{R}$ and afterwards integrated over the burned and unburned domains $\Omega^b(G')$ and $\Omega^u(G')$, respectively, to arrive at

$$\int_{\Omega^*(G')} r\left(\partial_t G + \left(u_j^* + \frac{\rho^u}{\rho^*}\right) \cdot \partial_j G\right)dA = 0. \tag{34}$$

In the following step, the burned and unburned realization of (34) are taken together, and the discretization in time is introduced. The application of the backward Euler scheme for the discretization in time results in the following semi-discrete system:

$$B^G(r, G^{n+1}; \Delta t|\mathbf{u}', G') = F^G(r; G^n, \Delta t|G'), \tag{35}$$

where the operators B^G and F^G are given by

$$B^G(r, G; \Delta t|\mathbf{u}', G') = \int_{\Omega^{G'}} r\left((\Delta t)^{-1}G + \left(u_j' + \frac{\rho^u}{\rho^*}\right) \cdot \partial_j G\right)dA \tag{36}$$

and

$$F^G(r; G, \Delta t|G') = (\Delta t)^{-1}\int_{\Omega^{G'}} r\,G^n\,dA, \tag{37}$$

respectively. The solution of (35) then corresponds to $G^{n+1} \in \mathcal{R}$ for which (35) holds for all $r \in \mathcal{R}$.

3.3. Finite element discretization

3.3.1. Interface capturing and numerical evaluation of the integrals

The domain Ω is discretized by a *non-deforming* triangular grid, resulting in the following triangulation $\mathcal{T}$:

$$\mathcal{T} = \left\{K \subset \Omega|\cup_{i=1}^{N_K} K_i = \Omega, K_i \cap K_j = \emptyset \text{ if } i \neq j\right\}. \tag{38}$$

Before introducing the enriched FEM in Section 3.3.2, we will first discuss the combined algorithm used to capture the interface I_f and construct the "integration cells", that are used for the evaluation of the integrals.

Rather than directly integrating over the elements as usual in FEM, it is customary in X-FEM that the integrals are evaluated using integration cells $S \subset K, K \in \mathcal{T}$ [46,16–18]. These integration cells have the property that they are either in the burned or the unburned part of the domain. Hence, the sign of the G-function $\text{sgn}(G)$ may be assumed constant over an integration cell. In this approach more integration points are introduced; however, we avoid having to numerically integrate discontinuous functions. As a consequence, the integrals, which are typically of the form $\int_{\Omega} f(\text{sgn}(G)) \, dA$, are evaluated as

$$\int_{\Omega} f(\text{sgn}(G)) \, dA = \sum_S \int_S f(\text{sgn}(<G>_S)) \, dA. \tag{39}$$

In order to avoid problems when determining the sign of the G-function very close to the interface where $G \approx 0$, the sign of the G-function in an integration cell is based on the average of G over the integration cell $\langle G \rangle_S = |S|^{-1} \int_S G \, dA$. Here $|S|$ denotes the surface of the integration cell. In the present implementation the integration surfaces S are either triangles or quadrilaterals and 5th order Gaussian integration schemes are used to evaluate these integrals.

The algorithm used to construct these integration cells is simultaneously used to capture the flame interface for which the algorithm provides a set of lines ℓ that eventually constitute the approximate flame interface $\mathcal{I}_f$. The complete algorithm is described in Algorithm 1. Similar algorithms can be found in, e.g. [46,16–18]. However, Algorithm 1 differs from earlier realizations in that it is also used to capture the flame interface.

Algorithm 1. Interface capturing and construction of integration cells

```
1:   for all Elements K ∈ 𝒯 do
2:       Initialize the set integration cells over K : 𝒮_K = {K}
3:   end for
4:   for i = 1 to N_refine do
5:       for all Elements K ∈ 𝒯 do
6:           for all Integration cells S ∈ ℐ_K do
7:               if Integration cell S is intersected by the line G = 0 then
8:                   Refine integration cell and update 𝒮_K
9:               end if
10:          end for
11:      end for
12:  end for
13:  Reset the set of line-elements that will later constitute the approximate interface ℐ_f = ∅
14:  for all Elements K ∈ 𝒯 do
15:      for all Integration cells S ∈ 𝒮_K do
16:          if Integration cell is intersected by the line G = 0 then
17:              1. Determine the line ℓ = I_f^G ∩ S using linear interpolation.
18:              2. Add ℓ to ℐ_f
19:              3. Divide integration cell S into two integration cells, one on each side of ℓ and update 𝒮_K
20:          end if
21:      end for
22:  end for
```

Summarizing, Algorithm 1 provides us with

(i) a set of non-overlapping integration cells $\mathcal{S}_K$ for each element $K \in \mathcal{T}$:

$$\mathcal{S}_K = \{S \subset K | \cup_i S_i = K, S_i \cap S_j = \emptyset \text{ if } i \neq j, \ \text{sgn}(G)|_S = \text{const.}\} \tag{40}$$

(ii) a set of lines $\ell \in \mathcal{I}_f$ constituting the approximate flame interface.

Afterwards, based on the sets of integration cells $\mathcal{S}_K, K \in \mathcal{T}$, two sets of lines, $\mathcal{G}_N$ and $\mathcal{G}_{D_{LM}}$, are extracted over the boundaries: Γ_N and $\Gamma_{D_{LM}}$, respectively. These sets are needed to evaluate the integrals over Γ_N and $\Gamma_{D_{LM}}$ and are given by

$$\mathcal{G}_N = \{\ell \neq \emptyset | \ell = \partial S \cap \Gamma_N, S \in \mathcal{S}_K, K \in \mathcal{T}\}, \tag{41}$$
$$\mathcal{G}_{D_{LM}} = \{\ell \neq \emptyset | \ell = \partial S \cap \Gamma_{D_{LM}}, S \in \mathcal{S}_K, K \in \mathcal{T}\}. \tag{42}$$

Similar to the integration cells, it may be assumed that lines $\ell \in \mathcal{G}_N, \mathcal{G}_{D_{LM}}$ are either in the burned or the unburned part of the domain.

Algorithm 1 is graphically illustrated in Fig. 2. First, as shown in Fig. 2(a), the initial integration cells are constructed, one for each element. Then, in a number of refinement steps, those integration cells that are intersected by the interface are

refined as shown in Fig. 2(b). In these figures the line $G = 0$ is represented by the thin dashed line. In the final step (Fig. 2(c)) the interface capturing takes place. Those integration cells that are intersected by the interface after the final refinement step are again divided into smaller integration cells, one on each side of the (approximate) interface. As can be seen in Fig. 2(c), this approach also provides an accurate capturing of the flame interface. In case linear elements are used to approximate the G-function, the additional refinement steps are not required, as the element-wise interface is a straight line in this case. Finally, all Gauss-points used for the evaluation of the integrals are shown in Fig. 2(d).

3.3.2. Enriched finite element method

Up to now we have considered two deforming (i.e., dependent on G) functional spaces for the velocity: $\mathcal{V}_g^u$ and $\mathcal{V}_g^b$. However, the actual discretization will be based on two other spaces. One *non-deforming* space $\overline{\mathcal{V}}_g$ with global support and a deforming enriched finite element space $\mathcal{V}'$ whose support is restricted to a region $\mathcal{D} \supset \mathcal{I}_f$, where we assume that $\mathcal{D} \cap \Gamma_{D_0} = \emptyset$. Analogously, the discretization of the pressure will be based on spaces $\overline{\mathcal{Q}}$ and $\mathcal{Q}'$.

The main advantage is that $\overline{\mathcal{V}}_g$ and $\overline{\mathcal{Q}}$ are independent of G and do not deform in time. The complete dependence on the G-function for the discretization of the variables is incorporated into the computational subspaces $\mathcal{V}'$ and $\mathcal{Q}'$, which only affect the discretization in a small region $\mathcal{D}$ near the interface.

For the non-deforming part of the discretization quadratic elements are defined over the triangular grid $\mathcal{T}$. Let $\mathcal{N}_0$ denote the resulting set of nodes k with nodal coordinates $\hat{\mathbf{x}}_k$ and shape functions $\phi_k, \phi_k \in H^1(\Omega) \cap C^0(\Omega)$, such that $\phi_k(\hat{\mathbf{x}}_j) = \delta_{kj}, k, j \in \mathcal{N}_0$.

Next we will describe the enriched shape functions. In the present paper we restrict ourself to an X-FEM discretization whose shape functions of the variables will be based entirely on the base set of nodes $\mathcal{N}_0$ and their shape functions. In this way, an X-FEM discretization for an arbitrary variable f is given by

$$f^h = \sum_{k \in \mathcal{N}_0} \hat{f}_k^0 \phi_k + \sum_{k \in \mathcal{N}_{enr}^a} \hat{f}_k^a \Theta^a \phi_k + \sum_{k \in \mathcal{N}_{enr}^b} \hat{f}_k^b \Theta^b \phi_k + \cdots \tag{43}$$

Here $\hat{f}^0, \hat{f}^a, \hat{f}^b, \ldots$ are the expansion coefficients, $a, b, \ldots$ are various types of enrichments and $\mathcal{N}_{enr}^a \subset \mathcal{N}_0, \mathcal{N}_{enr}^b \subset \mathcal{N}_0, \ldots$ are subsets of the base set of nodes $\mathcal{N}_0$ containing those nodes that are enriched. Further, $\Theta^a, \Theta^b, \ldots$ are the shape-modifying functions, that, e.g. modify the original shape function in such a way that discontinuities or kinks can be introduced. We
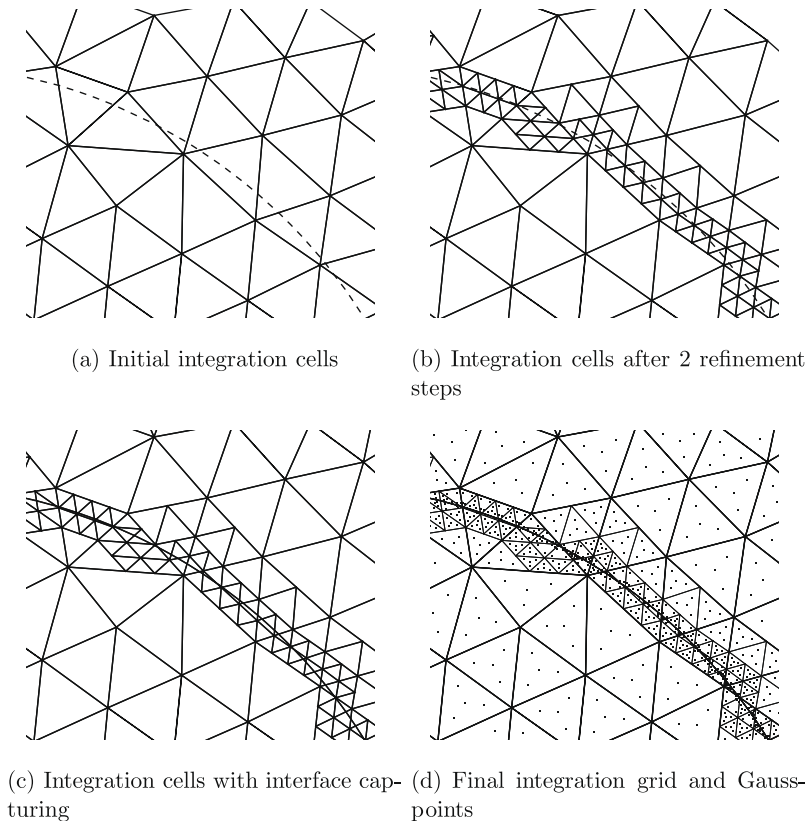

(a) Initial integration cells

(b) Integration cells after 2 refinement steps

(c) Integration cells with interface capturing

(d) Final integration grid and Gauss-points

Fig. 2. Graphical illustration of Algorithm 1 and the final evaluation points used in the evaluation of the integrals.

should emphasize that the X-FEM is formally not restricted to enrichments based on modifications of the shape functions $\phi_k, k \in \mathcal{N}_0$ as adopted here. However, in practise they often are.

In this paper we consider two types of enrichment, both introducing discontinuities across the interface. The first enrichment solely depends on the sign of the G-function, while the second one only contributes to the burned velocity and introduces a local coordinate transformation from Cartesian coordinates to the local coordinate system described by the G-function: $[\mathbf{n}, \tau]$. Hence, this later enrichment is highly affected by the local flame topology. We will refer to these enrichments as the jump-enrichment (J) and "topological" enrichment (top), respectively.

The set of nodes that is enriched using the jump-enrichment $\mathcal{N}_{\text{enr}}^J$ is given by

$$\mathcal{N}_{\text{enr}}^J(G) = \left\{ k \in \mathcal{N}_0 | \exists \mathbf{y} \in I_f(G) : |N_k(\mathbf{y})| > \varepsilon_J \right\} \tag{44}$$

with $\varepsilon_J \geqslant 0$, while the modifier-function Θ^J is defined as

$$\Theta^J(G) = \frac{1}{2}\,\text{sgn}(G) \tag{45}$$

and has the property $[\![\Theta^J]\!] = 1$. This well-known enrichment is used for both the pressure and the velocity field.

The "topological" enrichment is only applied to the velocity field and shows similarities with so-called tip-enrichments often encountered in X-FEM for crack-problems [47]. Hence, this enrichment is only applied to those nodes k around which the flame interface is highly curved within the support of ϕ_k. This curvature is determined by computing the maximal angle between the interface-normals $\mathbf{n}^\ell = \mathbf{n}|_\ell$ for those interface parts $\ell \in \mathcal{I}_f$ that lie within the support of ϕ_k. The resulting set of nodes $\mathcal{N}_{\text{enr}}^{\text{top}}$ that is "topologically" enriched is given by

$$\mathcal{N}_{\text{enr}}^{\text{top}}(G) = \left\{ k \in \mathcal{N}_0 | \max_{\ell_i, \ell_j \in \mathcal{I}_f \cap \text{supp}\phi_k} \cos^{-1}(\mathbf{n}^{\ell_i} \cdot \mathbf{n}^{\ell_j}) > \alpha_{\text{top}} \right\}, \tag{46}$$

where $\alpha_{\text{top}} > 0$ is a critical angle. The shape-modifying function for this enrichment Θ^{top} is defined as

$$\Theta^{\text{top}}(G) = [\mathbf{n}\tau]H(G). \tag{47}$$

Here H is the Heaviside function, and $[\mathbf{n}, \tau]$ is the local coordinate system determined by the G-function. Because $\Theta^{\text{top}}(G) \equiv 0$ on Ω^u, this enrichment only contributes to the burned velocity and introduces a local coordinate transformation from Cartesian coordinates to a coordinate system $[\mathbf{n}, \tau]$ related to the local flame topology. Some typical situations for which this enrichment is intended are shown in Fig. 3. In all these figures the burned velocity field is, contrary to the unburned velocity field, highly affected by the local flame topology.

The discretized velocity $\mathbf{u}^h$ and pressure p^h can now be expressed as

$$\mathbf{u}^h = \sum_{k \in \mathcal{N}_0} \hat{\mathbf{u}}_k^0 \phi_k + \sum_{k \in \mathcal{N}_{\text{enr}}^J} \hat{\mathbf{u}}_k^J \Theta^J \phi_k + \sum_{k \in \mathcal{N}_{\text{enr}}^{\text{top}}} \hat{\mathbf{u}}_k^{\text{top}} \Theta^{\text{top}} \phi_k, \tag{48}$$

$$p^h = \sum_{k \in \mathcal{N}_0} \hat{p}_k^0 \phi_k + \sum_{k \in \mathcal{N}_{\text{enr}}^J} \hat{p}_k^J \Theta^J \phi_k, \tag{49}$$

(a) Bunsen burner   (b) Circular flame   (c) One dimensional
                                                        flame with two fronts
                                                        moving towards each-
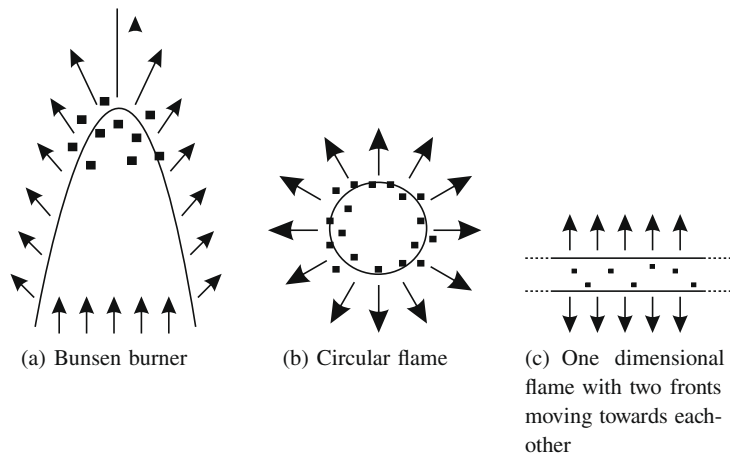   other

Fig. 3. Typical situations for which the enrichment based on the local flame topology is adopted: (a) At the tip of a Bunsen burner flame, (b) nodes around a circular flame and (c) one-dimensional flame with two fronts moving towards each other. In these figure "topologically" enriched nodes are indicated with ■. The arrows give an indication of the velocity field.

where $\hat{\mathbf{u}}_k^0, \hat{\mathbf{u}}_k^J, \hat{\mathbf{u}}_k^{\text{top}}, \hat{p}_k^0$ and $\hat{p}_k^J$ are the expansion coefficients. In Appendix A a proof is given showing that the above-introduced (enriched) shape functions $\phi_k, \phi_k \Theta^J$ and $\phi_k \Theta^{\text{top}}$ are linearly independent.

Finally, for the discretization of the G-function use is made of (unenriched) quadratic finite elements. Hence, the discretized G-function $G^h \in \mathcal{R}^h$ is given by

$$G^h = \sum_{k \in \mathcal{N}_0} \hat{G}_k \phi_k, \tag{50}$$

where $\hat{G}_k$ denote the expansion coefficients.

3.3.3. Discretization of the Lagrange multipliers

For the discretization of Lagrange multipliers over embedded interfaces, various techniques have already been proposed, see, e.g. Moës al. [7]. Therein the Lagrange multipliers are discretized *over* the interface, and all successful realizations of these methods have been restricted to two-dimensional problems. In fact, as will be motivated below, these methods will be very difficult to apply to three-dimensional problems. This is the reason why the distributed Lagrange multiplier (DLM) technique is adopted in this paper. This approach does not pose any fundamental problem in three dimensions. In the context of X-FEM, the use of the DLM technique was recently proposed by Kölke-Zilian and Legay [21,20]. As was already noted by those researchers, the DLM technique does provide a uniqueness issue, as the functions are defined over $\mathbb{R}^2$ but only evaluated over the one-dimensional interface. We propose a small modification of the interface in the form of stitches, which suffices to ensure a unique solution and shows proper convergence in a spatial convergence test.

The main problem when discretizing Lagrange multipliers *over* the interface is the need to construct a global coordinate system over the interface as well as a search algorithm to connect all individual interface parts, $\ell \in \mathcal{I}_f$. For large-scale three-dimensional problems, the latter problem can be overcome, at some computational expense. However, the former poses more severe difficulties, particulary when considering the highly irregular shape a turbulent flame can attain. Both the construction of a coordinate system related to the interface as well as a search algorithm to connect all individual interface parts $\ell \in \mathcal{I}_f$ are not required for the DLM technique. Hence, this method can also be adopted to three-dimensional problems without the need for introducing ad-hoc and problem-specific algorithms to arrive at a proper coordinate system.

The DLM technique provides an "implicit" definition [21] for the discretization of Lagrange multipliers. Instead of constructing nodes and shape functions over the flame interface and $\Gamma_{D_{LM}}$ the discrete Lagrange multipliers $(\lambda_n^h, \lambda_\tau^h)$ and (π_n^h, π_τ^h) are defined using subsets of the base node set $\mathcal{N}_0$ and its shape functions ϕ_k, i.e.,

$$\lambda_n^h = \sum_{k \in \mathcal{N}_\lambda} \hat{\lambda}_n \phi_k, \tag{51}$$

$$\lambda_\tau^h = \sum_{k \in \mathcal{N}_\lambda} \hat{\lambda}_\tau \phi_k, \tag{52}$$

$$\pi_n^h = \sum_{k \in \mathcal{N}_\pi} \hat{\pi}_n \phi_k \tag{53}$$

and

$$\pi_\tau^h = \sum_{k \in \mathcal{N}_\pi} \hat{\pi}_\tau \phi_k. \tag{54}$$

Here $\mathcal{N}_\lambda$ and $\mathcal{N}_\pi$ are subsets of $\mathcal{N}_0$, which, in the present implementation, are, respectively, defined as $\mathcal{N}_\lambda = \mathcal{N}_J$ and

$$\mathcal{N}_\pi = \left\{ k \in \mathcal{N}_0 | \mathbf{x}_k \in \Gamma_{D_{LM}} \right\}. \tag{55}$$

In order to explain the difficulties associated with the use of the DLM technique, let $\Lambda_f^h \subset \overline{\mathcal{V}} \cap \Lambda_f$ denote the discrete subspace associated with the discretization of the Lagrange multipliers. This space can formally be described as

$$\Lambda_{I_f}^h = \left\{ \left(\lambda_n^h, \lambda_\tau^h \right) |_{I_f} \Big| \lambda_i = \sum_{k \in \mathcal{N}_\lambda} \hat{\lambda}_{ik} \phi_k; \hat{\lambda}_{ik} \in \mathbb{R} \right\}. \tag{56}$$

As can be inferred from (56), the distributed Lagrange multipliers λ_n^h and λ_τ^h are only evaluated at the interface. However, the functions ϕ_k used for their discretization have a support in $\mathbb{R}^2$ which results in non-unique solutions. To illustrate this, consider the following one-dimensional example for which we assume a base discretization $\mathcal{N}_0$ consisting of two nodes located at the endpoints of a domain $[0, 1]$ and an interface located at $x_I \in]0, 1[$. The shape functions ϕ_k are given by $\phi_1 = 1 - x$ and $\phi_2 = x$, respectively, such that a Lagrange multiplier λ is discretized as $\lambda^h(x) = \hat{\lambda}_1(1 - x) + \hat{\lambda}_2 x$. One can readily verify that $\lambda^h(x_I) = 0$ for all functions λ^h for which $\hat{\lambda}_2 = -(1 - x_I)\hat{\lambda}_1 / x_I$. A number of realization of functions λ^h with $\lambda^h(x_I) = 0$ are shown in Fig. 4. As a consequence, the null-space $\text{Ker}(\Lambda_f^h)$ has dimension one, and consequently the final matrix system cannot be of full rank, resulting in a non-unique solution of the saddle-point problem.

This problem is also encountered in the two-dimensional case as studied in this paper and an example can be given when the level-set function G can be approximated by linear basis functions and the flame interface is a straight line. Because G can be approximated by linear basis functions, the vector $(G^h, G^h) \in \Lambda_{I_f}^h$. Now by definition, over the interface $G^h = 0$, however,
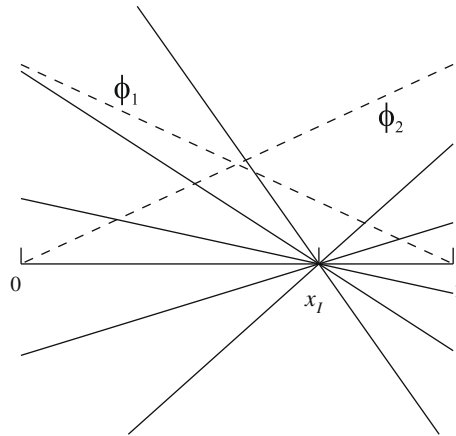
Fig. 4. A collection of functions $\lambda^h = \hat{\lambda}_1 \phi_1 + \hat{\lambda}_2 \phi_2$ for which $\lambda^h(x_I) = 0$ (solid lines). The dashed lines indicated the shape functions $\phi_1 = 1 - x$ and $\phi_2 = x$.

there are expansion coefficients $\hat{G}_k$ that are non-zero. (In fact, most of the expansion coefficients will be non-zero.) Hence, the dimension of $\mathrm{Ker}(\Lambda_{I_f}^h)$ can also be non-zero in the general case.

In order to avoid this situation, we propose to slightly modify the approximate interface $\mathcal{I}_f$ by adding small "stitches" ℓ^s to the interface (see Fig. 5). In particular, we add a stitch ℓ^s at the midpoint of every $\ell \in \mathcal{I}_f$ of length $h_K/10$ oriented perpendicular (relative to the local element coordinate system) to the original line ℓ. For the one-dimensional example described above, the interface is now given by $I_f =]x_I - \varepsilon, x_I + \varepsilon[$, and it is no longer possible to find $\hat{\lambda}_1, \hat{\lambda}_2 \neq 0$ for which $\lambda^h(x) = 0, \forall x \in I_f$. Similar arguments can be given for the two-dimensional case.

Remarks.

(1) As indicated in the beginning of this section, our choice for the DLM technique as well as the modification of the interface via stitches is mainly motivated by practical reasons. However, in Section 4.2, results of a spatial convergence analysis are shown for various typical stitch lengths. These results demonstrate good convergence properties as long as the stitch length is chosen to be $\ell^s \approx h_K/10$.

(2) The integrals related to Lagrange multipliers on the interface as, e.g. encountered in (23) become somewhat more complex and are now evaluated as

$$\int_{\mathcal{I}_f} l_n^h [\![u_n^h]\!] \, dS = \sum_{k \in \mathcal{N}_\lambda} \sum_{\ell_i \in \mathcal{I}_f} \hat{l}_{nk} \Bigg\{ \sum_{l \in \mathcal{N}_{\mathrm{enr}}^J} \left(\int_\ell \phi_k \phi_l [\![\Theta_{\mathrm{enr}}^J]\!] \, dS + [\![\Theta_{\mathrm{enr}}^J]\!] \big|_{\mathbf{x}^s} \int_{\ell^s} \phi_k \phi_l \, dS \right) \hat{u}_{nl}^J$$

$$+ \sum_{l \in \mathcal{N}_{\mathrm{enr}}^{\mathrm{top}}} \left(\int_{\ell_i} \phi_k \phi_l [\![\Theta_{\mathrm{enr}}^{\mathrm{top}}]\!] \, dS + [\![\Theta_{\mathrm{enr}}^{\mathrm{top}}]\!] \big|_{\mathbf{x}^s} \int_{\ell^s} \phi_k \phi_l \, dS \right) \hat{u}_{nl}^{\mathrm{top}} \Bigg\}, \tag{57}$$
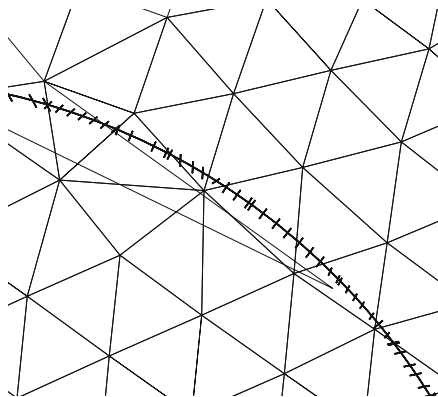

Fig. 5. Graphical illustration of the stitches corresponding to the grid shown earlier in Fig. 2.

where $\mathbf{x}^s$ is the point where the stitch ℓ_i^s intersects ℓ_i. The terms $[\![\Theta_{\mathrm{enr}}^J]\!]$ and $[\![\Theta_{\mathrm{enr}}^{\mathrm{top}}]\!]$ are evaluated at this point and out-side the integral, as $[\![\Theta_{\mathrm{enr}}]\!] = 0$ on $\ell^s \setminus \mathbf{x}^s$. Evaluating these terms inside the integral would cancel out the effective sta-bilizing mechanism which is incorporated in $\int_{\ell^s} \phi_k \phi_l \, dS$.

(3) In practise, we only encountered the above described problem of a null-space $\mathrm{Ker}(\Lambda_{l_f}^h)$ of non-zero dimension in cases where G can indeed be approximated by linear basis functions and the interface is a straight line. Already a slightly curved interface was sufficient to arrive at a matrix of full rank. However, the condition number of the resulting matrix was very high. With the introduction of stitches to the interface, the condition number of the resulting matrix could be considerably decreased.

3.3.4. Residual based stabilization for the fluid equation system

For the stabilization of (28) we rely on an SUPG/PSPG stabilization in combination with a grad-div stabilization, see, e.g. [48,49]. Therefore the stabilization terms $B^{F,stab}(\mathbf{W}, \mathbf{U}^{n+1,s}; \mathbf{u}^{n+1,s-1}, \Delta t | G')$ and $F^{F,stab}(\mathbf{W}; \mathbf{u}^{n+1,s-1}, \mathbf{u}^n, \Delta t | G')$ are added to the left and right hand side of (31), respectively. The stabilization operators $B^{F,stab}$ and $F^{F,stab}$ are given by

$$B^{F,stab}(\mathbf{W}, \mathbf{U}; \boldsymbol{\beta}, \Delta t | G) = \sum_{K \in \mathcal{T}} \delta_K \int_K \rho^{-1}(\beta_j \cdot \partial_j w_i + \partial_i q) \times \left((\Delta t)^{-1} \rho u_i + \rho \beta_j \partial_j u_i + \partial_i p - \mu \partial_j \epsilon_{ij}(\mathbf{u}) \right) dA$$

$$+ \gamma_K \int_K \rho (\nabla \cdot \mathbf{w})(\nabla \cdot \mathbf{u}) \, dA, \tag{58}$$

$$F^{F,stab}(\mathbf{W}; \boldsymbol{\beta}, \mathbf{u}^n, \Delta t | G) = \sum_{K \in \mathcal{T}} \delta_K \int_K \rho^{-1}(\beta_j \cdot \partial_j w_i + \partial_i q)(\Delta t)^{-1} \rho u_i^n \, dA. \tag{59}$$

Here the elements-wise constants δ_K and γ_K are defined as

$$\delta_K = \min \left(\Delta t, \frac{h_K}{2\|u\|_{2,K}}, \frac{m_K h_K^2}{4v} \right), \tag{60}$$

$$\gamma_K = \min \left(\frac{1}{2} h_K \|u\|_{2,K}, \frac{m_K h_K^2 \|u\|_{2,K}^2}{4v} \right), \tag{61}$$

respectively, where $v = \rho^{-1}\mu$ is the kinematic viscosity, h_K is the maximal diameter of K and the constant m_K is set to $\frac{1}{12}$ for the quadratic elements used.

3.3.5. Edge-based stabilization for the G-function

For the stabilization of the G-function, an edge-based stabilization technique is used. The stabilization technique penal-izes jumps in the gradients $[\![\mathbf{n} \cdot \nabla G]\!]_e$ across the edges $e = \partial K_L \cap \partial K_R$ shared by two neighboring elements $K_L, K_R \in \mathcal{T}$. Here $[\![f]\!]_e = f^L - f^R$ is the jump operator at the edge e whose traces f^L and f^R are defined as $f^L(\mathbf{y}) = \lim_{\varepsilon \downarrow 0} f(\mathbf{y} - \varepsilon \mathbf{n}^L)$ and $f^R(\mathbf{y}) = \lim_{\varepsilon \downarrow 0} f(\mathbf{y} - \varepsilon \mathbf{n}^R)$, respectively. Here $\mathbf{y} \in e$, while $\mathbf{n}^L$ and $\mathbf{n}^R$ denote the outward-pointing normals with respect to K_L and K_R, respectively. Edge-based stabilization techniques have originally been proposed in [38] and have received consider-able attention in recent years in the work of Burman et al. [39,40].

The choice of an edge-based stabilization for the G-function is not arbitrary and is closely linked to the signed-distance property (11). When not using C_1-regular finite elements, such as Hermite and Argyris elements [50], conforming finite ele-ments will develop kinks across the element edges. This results in large discrepancies in the gradient magnitude of neighbor-ing elements which conflicts with the signed-distance property. Kinks across element edges are penalized by the edge-based stabilization enforcing a solution with a more uniform gradient magnitude. As implied by (11), such a uniform gradient mag-nitude is a fundamental property of a level-set function.

This stabilization results in the addition of the following term to the left hand side of (35):

$$B^{G,stab}(r, G^{n+1,s} | \mathbf{u}', G') = \sum_{e \in \mathcal{E}} \gamma_e h_e^2 \int_e [\![\mathbf{n}^e \cdot \nabla r]\!]_e [\![\mathbf{n}^e \cdot \nabla G^{n+1,s}]\!]_e \, dS, \tag{62}$$

where $\gamma_e = c_2 \|\mathbf{u}' \cdot \mathbf{n}^e\|_{e,\infty}$ [40] and $\mathcal{E}$ is the set containing all shared edges

$$\mathcal{E} = \{e \neq \emptyset | e = \partial K_L \cap \partial K_R; K_L \neq K_R, K_L, K_R \in \mathcal{T}\}. \tag{63}$$

Further, in (62) h_e denotes the length of the edge e, $\mathbf{n}^e = \mathbf{n}^L$ the normal associated with e and $\|\cdot\|_{e,\infty}$ denotes the maximum norm over e. The constant c_2 is set to $\frac{1}{10}$ [40].

3.4. Fluid-G-function interaction

A description of the iteration technique used for the fluid-G-function interaction (FGI) is given in Algorithm 2. The basic structure of this algorithm is similar to algorithms used in fluid-structure interaction (FSI). As convergence criterion we adopt

$$\|G^{n+1} - G'\|^2 = \int_{\Omega} (G^{n+1} - G')^2 \, d\mathcal{A}, \tag{64}$$

where G' is the G-function obtained as a result of the previous iteration. As can be observed in Algorithm 2 the enrichment is no longer updated when the convergence norm (64) has reached $\varepsilon' > \varepsilon$. This is done to avoid a cyclic loop when the enrichment of a certain node is turned on and off after each FGI-iteration. This occurs particulary when the interface is close to an element edge. For the results presented in the following section, we have adopted $\epsilon = 10^{-6}$ and $\epsilon' = 10^{-4}$.

Algorithm 2. Fluid-G-function interaction

```
1:   for each timestep t_{n+1} do
2:       Reinitialize G
3:       while ‖G^{n+1} − G′‖ < ε do
4:           1. Determine new G^{n+1} using the current velocity field. As initialization for the G-function use the present
                realization of the G-function.
5:           2. Determine approximate interface I_f and integration surfaces using Algorithm 1 based on the new realization of
                G^{n+1}
6:           if ‖G^{n+1} − G′‖ < ε′ then
7:               3. Update enriched nodes
8:           end if
9:           4. Determine new velocity field u^{n+1}. For the initialization of the non-linear iteration, use the latest velocity field.
10:      end while
11:  end for
```

In order to keep the G-function as close as possible to a signed-distance function, at the beginning of each timestep, the level-set equation is re-initialized based on (11). Hence, we adopt a direct approach instead of usual reinitialization methods, that rely on pseudo-timestepping techniques. Next to some stability issues, the direct approach turned out to require less computing time than usual re-initialization methods as used in [51–53].

4. Results

In this section a number of results are shown to verify the method and our implementation. We will show results for particular flames that were investigated in papers by Nguyen et al. [26] and by Law and co-workers [32–35]. As a final test case, we consider a piloted Bunsen burner flame to show the potential of this method when applied to more complex problems. Throughout this section, we adopt $\rho^u = 1.0, \rho^b = 0.2, \varepsilon^J = 10^{-6}$ and $\alpha^{\text{top}} = 60°$, unless otherwise noted.

4.1. Moving flame fronts

We will first show results of two flame fronts initially located at $x_1 = 0.04$ and $x_1 = 3.96$ in a domain $[0, 4] \times [0, 1]$ with the unreacted material at rest in between the two flame fronts. These two flame fronts will move towards each other. The simulation is stopped as soon as all unreacted material is gone and the flame fronts have collided. In the x_2-direction, we consider periodic boundary conditions, while at $x_1 = 0$ and $x_1 = 4$ zero-pressure outflow boundary conditions are used. Further, $\mu^u = \mu^b = 1000$ and the flamespeed is given by $s_L = 1$. For the results shown, in total 400 elements with a characteristic element length of $h = 0.2$ are used. The timestep Δt is set to 0.01

First, in Fig. 6(a) and (b), an impression is given of the grid, the flame front and the enriched nodes around the flame interface at $t = 0.5$ and $t = 1.8$, respectively. As can be observed, the interface remains perfectly straight during the simulation. This is also observed in Fig. 7, where the velocity in the x_1-direction and the pressure are shown at two instances in time. In these plots the actual values of the velocity and pressure at the Gaussian integration points are shown and, as can be seen, we achieve an extremely accurate representation of the jump across the interface. Finally, in Fig. 8, we show the x_1-coordinate of the upper and lower flame front as a function of time. Also in this figure, we depict the number of nodes that are enriched using the jump and topological enrichment, respectively. One can observe that the topological enrichment is only activated when the flame fronts come very close to each other (compare with Fig. 3(c)). Moreover, the use of this enrichment has no effect on the speed with which flame fronts are moving towards each other before finally colliding.

4.2. Darrieus–Landau instability

A second well-documented flow that can be used to verify the method introduced in this paper is the hydrodynamic or Darrieus–Landau instability [26,32,34,35]. As shown in, e.g. [54], a straight flame interface which is perturbed by a small perturbation with wave-number k and initial amplitude A_0 will become unstable. The amplitude A will grow exponentially in time with an exponential growth rate ω given by,

$$\omega = \frac{ks_L}{1 + \rho^b/\rho^u} \left(-1 + \sqrt{1 + \frac{\rho^u}{\rho^b} - \frac{\rho^b}{\rho^u}} \right). \tag{65}$$

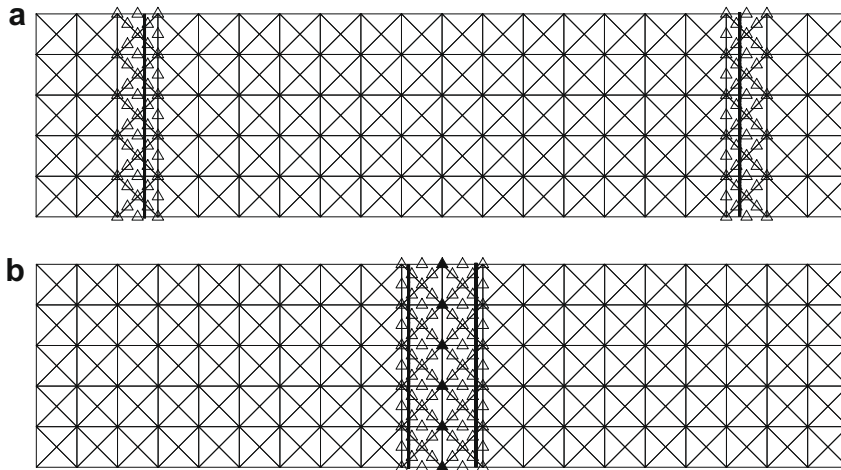**Fig. 6.** Grid, flame front (thick black line) and enriched nodes (△ and ▲) at (a) $t = 0.5$ and (b) $t = 1.8$. Nodes enriched by both the jump and the topological enrichment are indicated by ▲.
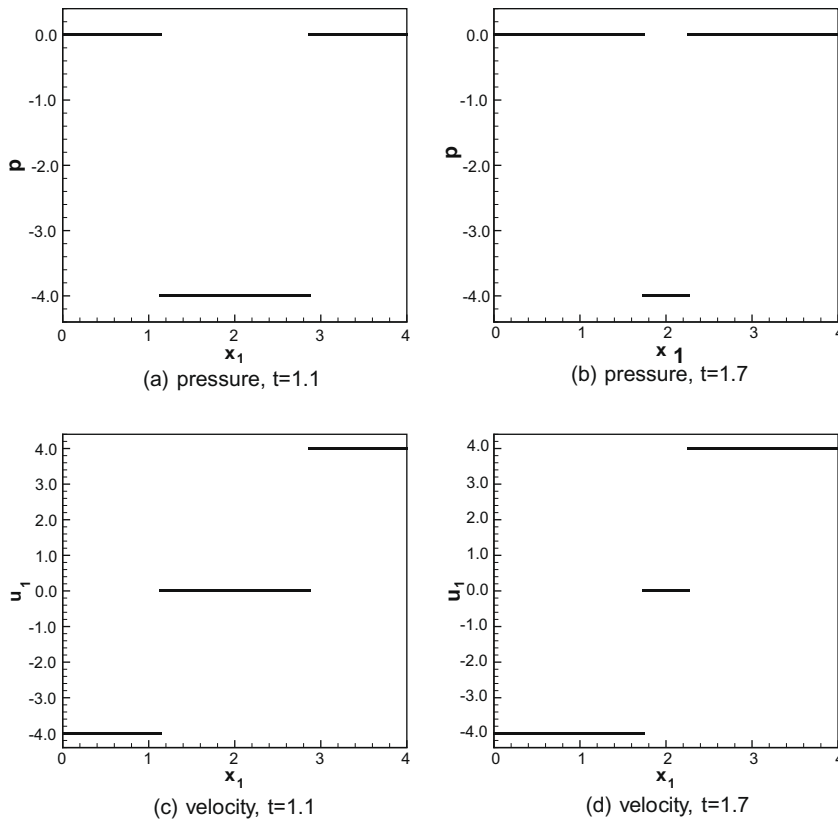

Fig. 7. Velocity in x_1-direction and pressure evaluated at the Gaussian integration points for two instances in time.

In the first part of this subsection, we investigate to what extend the method is capable of reproducing this growth rate for various ratios ρ^b/ρ^u. In the second part of this subsection, results of a spatial convergence test are shown. where we establish the effectiveness with which the DLM technique is capable of enforcing the boundary conditions over the interface.

We consider the same case as studied in, e.g. [32,34,35], such that $\mu^u = 0.011, \mu^b = 0.035$ and $s_L = 1.0$, while various ratios of ρ^u/ρ^b are used. The wave-number of the perturbation is set to $k = 5$ and the domain is given by $\Omega = \left[0, \frac{2\pi}{5}\right] \times \left[0, \frac{2\pi}{5}\right]$. In the first part of this subsection, we consider a fixed grid with 1024 elements such that the typical element length $h = \frac{2\pi}{80}$ Further, the initial wave amplitude A_0 is set to 10^{-2} times the wave-length of the perturbation. For the spatial convergence study
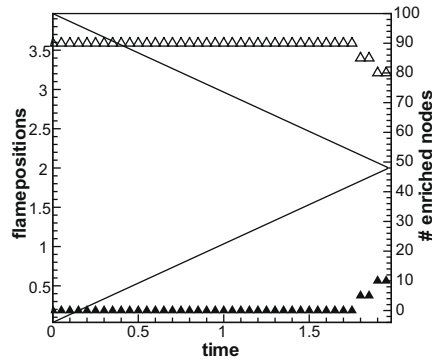
Fig. 8. Location of the two flame fronts as a function of time (solid). With △ and ▲, we indicate the number of nodes that are enriched with the jump and topological enrichment, respectively.

the resolution as well as the initial amplitude A_0 are varied. At the boundaries, we consider periodic boundary condition in the x_1-direction. A zero-pressure outflow boundary conditions is used at $x_2 = \frac{2\pi}{5}$, while a Dirichlet boundary condition with $\mathbf{g} = [0, 1]$ is used for the inflow located at $x_2 = 0$. Similar to [26] the initial guess for the velocity field $\mathbf{u}_0^* = [0, 1]$ is first iterated to a steady state without changing the position of the interface. Only after reaching this steady state the actual simulation is started with timestep $\Delta t = 0.001$.

In Fig. 9, the analytical growth rate (65) is compared with the growth rate of the amplitude obtained during simulations. These results show considerable differences when simulating with or without the edge-based stabilization for the level-set function in particular for large ratios of ρ^u/ρ^b. Without edge-based stabilization the interface will develop kinks (see
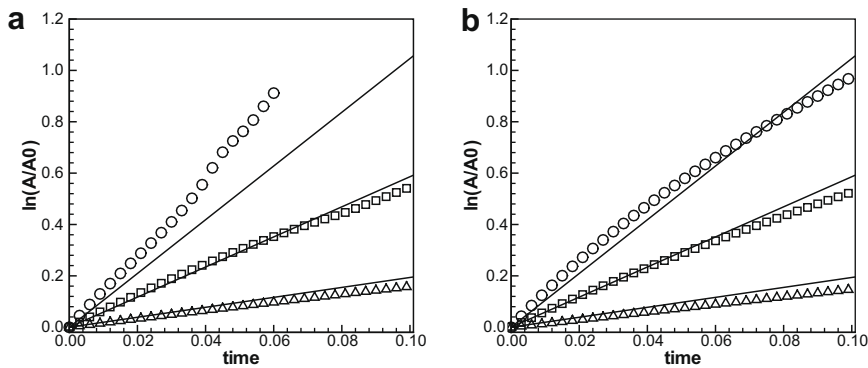

Fig. 9. Exponential growth rate ω of a perturbed flame front for $\rho^u/\rho^b = 2, 5$ and 10. Analytical growth rates (solid lines) and growth rate $\ln(A(t)/A_0)$ as determined from the simulations, $\rho^u/\rho^b = 10$ (circles), $\rho^u/\rho^b = 5$ (squares) and $\rho^u/\rho^b = 2$ (triangles): (a) no edge-based stabilization for the level-set function G, (b) with edge-based stabilization.
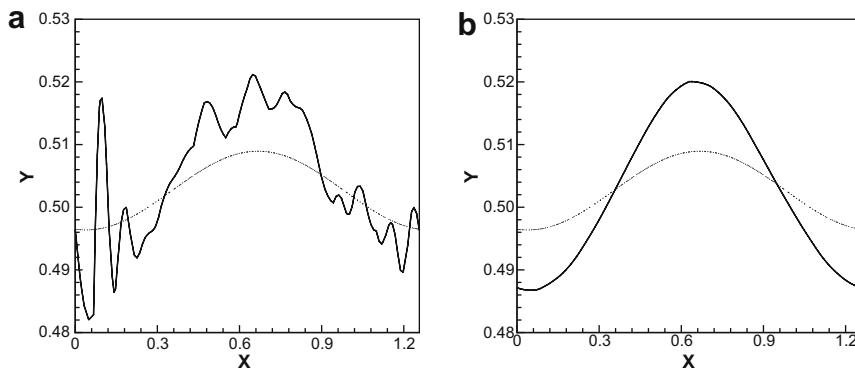

Fig. 10. Interface at $t = 0.1$ (solid) of an initially perturbed flame front (dotted) with $\rho^u/\rho^b = 10$: (a) no edge-based stabilization, (b) with edge-based stabilization.

Fig. 10(a)), which prevent an accurate prediction of the growth rate. In fact, the simulation with $\rho^u/\rho^b = 10$ turned out to be unstable due to these kinks. The development of these kinks is prevented when the edge-based stabilization is applied to the G-function, as can bee seen in Fig. 10(b). No kinks emerge, finally resulting in an accurate prediction of the growth rate.

For the spatial convergence study, we consider $\rho_b/\rho_u = 0.2$ and, at first, $|\ell^s|/h_K = 0.10$. Further, in order to avoid any influence from the time-stepping scheme, we only consider those results obtained from the steady-state initial field. In Fig. 11, the spatial convergence for the L_2-errors of the velocity jumps in the normal and tangential direction $[\![u_n]\!] - J_n$ and $[\![u_t]\!] - J_t$, respectively, are displayed. In these figures, results are shown for various amplitudes A_0. The observed convergence ranges from $h^{0.63-0.95}$ for the L_2-error in the normal direction and $h^{0.96-1.00}$ in the tangential direction. This difference is probably related to the more complex mixed boundary condition that is enforced over the interface in the normal direction. Due to the implicit nature of the shape functions, the actual shape and polynomial order of the shape functions at the interface are unknown. Hence, further analysis is required to relate the observed convergence rates to analytical/optimal convergence rates.

In order to study the effect of the stitch length, in Figs. 12 and 13 results are shown in which the stitch length is set to $|\ell^2|/h_J = 0.05$ and 0.15, respectively. As can be seen, better convergence is obtained when the stitch length is decreased. However, in this case a number of simulations could not be completed (the results for $N = 128^2$ are missing for $A_0 = 0.001$ and $A_0 = 0.01$ in Fig. 12). On the other hand, increasing the stitch length leads to considerably reduced convergence rates, especially in the normal direction.

4.3. Bunsen burner flame

Finally, results from the simulation of a piloted Bunsen burner flame are presented. These results are included to show the potential of the proposed method to handle flames in complex geometries. In the present paper, only a qualitative assessment of the results is included. Hence, we do not provide comparison with experimental data. The intension is to confront the presented method with experimental results in future work.

An overview of the grid and geometry adopted for the simulation is given in Fig. 14. We consider a domain of size $[-D, D] \times [-\frac{1}{2}D, 4D]$. Here D denotes the diameter of the main burner. The rim of the burner is located at $y = 0$ and the total diameter of the burner (main burner and co-flow) is 1.9 D. The small walls separating the individual flows have a thickness of
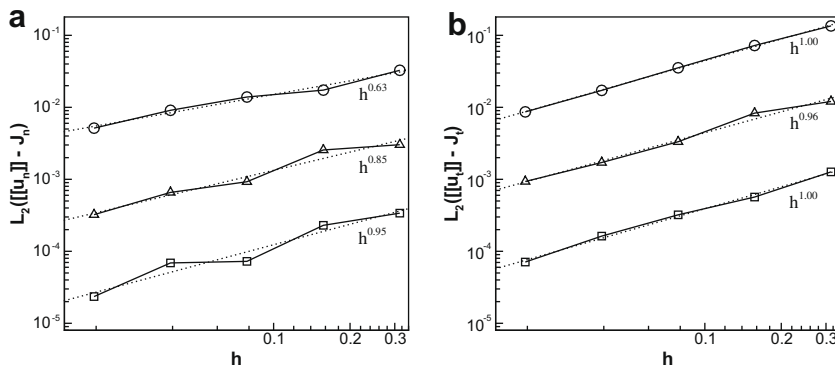

Fig. 11. Spatial convergence of (a) $L_2([\![u]\!]_n - J_n)$ and (b) $L_2([\![u]\!]_t - J_t)$ for various initial amplitudes $A_0 = 0.001(\bigcirc), A_0 = 0.01(\triangle)$ and $A_0 = 0.1$ ($\square$) and $|\ell^s|/h_K = 0.10$. The dotted lines represent the power fits.
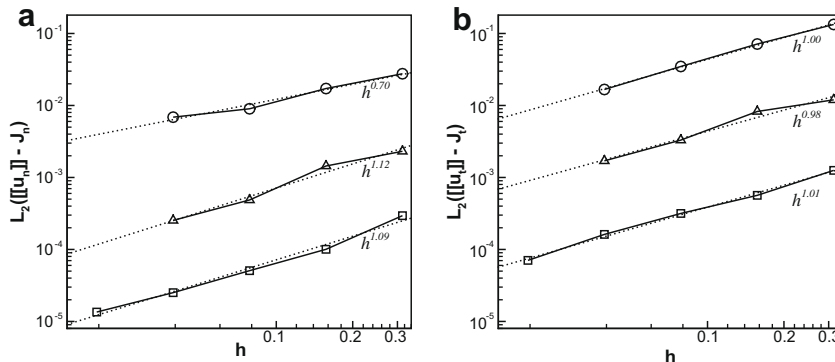

Fig. 12. Same as in Fig. 11 but with $|\ell^s|/h_K = 0.05$.

$\frac{1}{20}D$. At these walls, no-slip boundary conditions are used. As indicated in Fig. 14(a), over the inside of the main burner and on top of the walls between the main and co-flow, these boundary conditions are enforced using Lagrange multipliers. For the inflow at $y = -D/2$, we adopt $\mathbf{g} = [0.0, 1.0]$ for both the main burner as well as the co-flow and along the outflow boundaries zero-pressure Neumann boundary conditions are adopted. Finally, two points located at the edge of the burner rim: $(-\frac{1}{2}D, 0)$ and $(\frac{1}{2}D, 0)$, are used to fix the flame. Altogether, approximately 3700 elements are used.

The Reynolds number based on the inflow velocity and the diameter of the main burner is set to 100 for both unburned and burned gases and we adopt $\rho_u = 1.0$ and $\rho_b = 0.2$. Use is made of quadratic elements for the discretization of the velocity, the pressure as well as the G-function. The flame speed in the normal direction is defined as $s_n = 0.2f(y)$. Here, the function $f(y)$ is defined as

$$f(y) = \begin{cases} 0 & \text{if } y < 0 \\ 20y & \text{if } 0 \leqslant y < \frac{1}{20} \\ 1 & \text{else} \end{cases} \tag{66}$$

and is used to introduce a short transition region at the burner rim. Such a transition is needed, because near the wall $u_i^u = u_i^b = 0$ due to the no-slip boundary condition which does not allow for a discontinuous velocity field over the flame interface at the wall.

The flame is initialized with the circular flame of radius D and is allowed to develop up to $t = 1.6$. In Fig. 15(a) an overview is given of how the flame develops over this period. Further, results for the flame at $t = 1.6$ are shown in Figs. 15(b) and (c). In
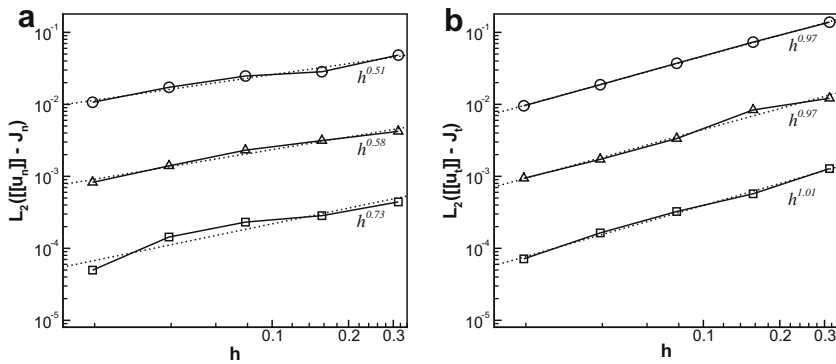

Fig. 13. Same as in Fig. 11 but with $|\ell^\delta|/h_K = 0.15$.
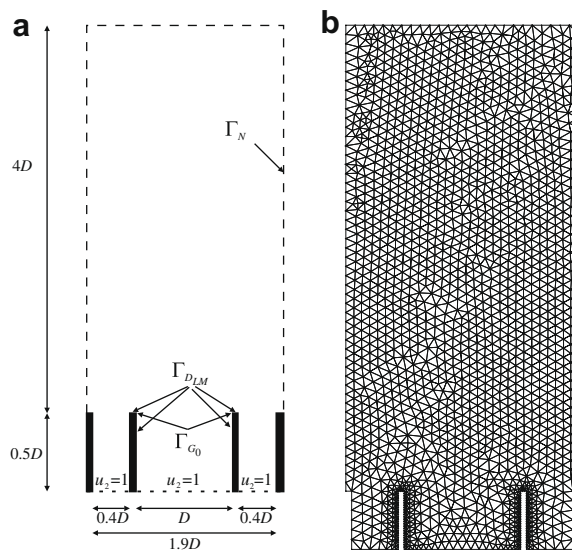

Fig. 14. An illustration of the domain and grid used for the simulation of the piloted Bunsen burner flame: (a) domain and boundary conditions, (b) grid. For those walls indicated by $\Gamma_{D_{LM}}$ the no-slip boundary conditions are enforced using Lagrange multipliers. Further, at the Burner rim two points $(-D/2, 0)$ and $(D/2, 0)$ indicated with Γ_{G_0} are used to fix the flame.

Fig. 15(b) an illustrative figure is shown of the shape of the flame together with a scatter plot of all nodes that are enriched near the interface. In Fig. 15(c) an impression of the velocity field is given. Here, the jump that the velocity field undergoes when crossing the flame interface can clearly be observed. The observed pattern of the streamlines is similar to that shown in, e.g. [55].

5. Conclusions

In this paper a novel approach to simulate premixed combustion based on the G-function approach has been introduced. In the G-function approach, the domain is divided into two parts, one containing the burned and another containing the unburned gases. A level-set or G-function is used to define the flame interface separating burned from unburned gases. We propose the use of an eXtended finite element method (X-FEM) that allows for a exact representation of the discontinuities encountered in velocity and pressure fields across the flame interface. With respect to the evolution of the flame interface, a standard FEM is used for the level-set function defining the interface. The approach presented in this paper has the advantage, compared to earlier methods used to simulate premixed turbulent combustion using the G-function approach, that neither smoothing of the discontinuities nor interpolation of the level-set function in between grid points is required.

The X-FEM has been applied to various problems ranging from crack problems in solid mechanics to fluid-structure interaction. In a number of the problem types dealt with using X-FEM, essential boundary conditions are encountered across the embedded interfaces. The general approach is to enforce these boundary conditions using Lagrange multipliers. However, the discretization of these Lagrange multipliers has been a persisting problematic issue. In the problem type dealt with in the current paper, this issue is even more intricate due to the very irregular shape a turbulent flame interface can attain.

Regarding the discretization of the Lagrange multipliers in the X-FEM context, the general approach is to construct shape functions over the interface. However, we are not aware of any such method that can be applied to three-dimensional problems. Discretizing the Lagrange multiplier using the distributed Lagrange multiplier method as recently proposed in [21,20], however, does not introduce any fundamental drawbacks in three dimensions. Exploiting the shape functions already defined and used for the discrete velocity and pressure fields, the distributed Lagrange multipliers method provides an implicit discretization of the Lagrange multipliers. However, as the Lagrange multipliers are only evaluated at the interface, the solution may not be unique. We have shown that this can be resolved by a slight modification of the interface in the form of "stitches". It is our intent to study and consider (alternative) techniques to ensure uniqueness in the future.

The level-set function used to track the interface is generally assumed to be a very smooth function. However, C^0-continuous finite element methods as used in the current paper may develop kinks across the element edges. Therefore, we have used the recently proposed edge-based stabilization technique that penalizes jumps in the gradients across shared edges and prevent large inter-element differences in the gradient magnitude. Results have shown that without the use of this stabilization technique it would not be possible to reproduce the analytical growth rate observed in the Darrieus–Landau instability.

In this paper, our current implementation has been analyzed for various test cases. Future work will, aside from the extension to three dimensions, mainly lie on the testing of the method for turbulent flames with flame wrinkling, flame-turbulence interaction etc. It is our intension to compare results of a piloted Bunsen burner flame with numerical and experimental data at high Reynolds number. Initial results from computations of a piloted Bunsen burner flame at moderate Reynolds number have already been included in the current paper.

Acknowledgment

Appendix A. Linear independency of the enriched shape functions

In order to check wether the enrichments introduced above are linearly independent, we introduce the following matrix:

$$
A = \begin{bmatrix} 1 & 0 \\ 0 & 1 \\ \frac{1}{2}\mathrm{sgn}(G) & 0 \\ 0 & \frac{1}{2}\mathrm{sgn}(G) \\ n_1 H(G) & n_2 H(G) \\ \tau_1 H(G) & \tau_2 H(G) \end{bmatrix},
\tag{A.1}
$$

which allows us to alternative express the enriched velocity as

$$
u_j^h = \sum_{k \in \mathcal{N}_0} \sum_{i=1}^{n_k^{dof}} \hat{u}_{ki} A_{ij} \phi_k.
\tag{A.2}
$$

Here n_k^{dof} is the number of degree of freedoms assigned to node k for the velocity field. Now in order to show under which conditions a node k which is enriched by both the jump and the topological enrichment ($n_k^{dof} = 6$) provides linearly independent basis functions we need to show that there are three points $\mathbf{x}_1, \mathbf{x}_2$ and $\mathbf{x}_3$ within the support of ϕ_k for which the block matrix

$$
\mathcal{A} = [A(\mathbf{x}_1)|A(\mathbf{x}_2)|A(\mathbf{x}_3)]
\tag{A.3}
$$

has full rank. Therefore, choose $\mathbf{x}_1$ in the unburned domain and that two other points $\mathbf{x}_2$ and $\mathbf{x}_3$ in the burned domain. Then the block matrix $\mathcal{A}$ is given by

$$
\mathcal{A} = \begin{bmatrix} 1 & 0 & 1 & 0 & 1 & 0 \\ 0 & 1 & 0 & 1 & 0 & 1 \\ -\frac{1}{2} & 0 & \frac{1}{2} & 0 & \frac{1}{2} & 0 \\ 0 & -\frac{1}{2} & 0 & \frac{1}{2} & 0 & \frac{1}{2} \\ 0 & 0 & n_1(\mathbf{x}_2) & n_2(\mathbf{x}_2) & n_1(\mathbf{x}_3) & n_2(\mathbf{x}_3) \\ 0 & 0 & -n_2(\mathbf{x}_2) & n_1(\mathbf{x}_2) & -n_2(\mathbf{x}_3) & n_1(\mathbf{x}_3) \end{bmatrix}
\tag{A.4}
$$

and one can readily observe that $\mathcal{A}$ is not off full rank iff $\mathbf{n}(\mathbf{x}_2) = \mathbf{n}(\mathbf{x}_3)$. However, by (46) a node may only adopt the topological enrichment if there are $\mathbf{x}_2$ and $\mathbf{x}_3$ for which $\mathbf{n}(\mathbf{x}_2) \neq \mathbf{n}(\mathbf{x}_3)$, hence, $\mathcal{A}$ is of full rank.

Remark: It should be noted that when the critical angle is chosen small ($\alpha^{top} < 10°$), the condition number of the matrix $\mathcal{A}$ is very large as the basis functions become nearly linearly dependent. Thus, it is advised to choose α relatively large (45 degrees or larger).

References

[1] N. Peters, Turbulent Combustion, Cambridge University Press, Cambridge, 2000.
[2] A.G. Class, B.J. Matkowsky, A.Y. Klimenko, A unified model of flames as gasdynamic discontinuities, J. Fluid Mech. 491 (2003) 11–49.
[3] F. Williams, Turbulent combustion, in: J. Buckmaster (Ed.), The Mathematics of Combustion, SIAM, Philadelphia, 1985, pp. 97–131.
[4] T. Belytschko, T. Black, Elastic crack growth in finite elements with minimal remeshing, Int. J. Numer. Methods Eng. 45 (5) (1999) 601–620.
[5] J. Chessa, T. Belytschko, A local space–time discontinuous finite element method, Comput. Methods Appl. Mech. Eng. 195 (2006) 1325–1343.
[6] J. Chessa, T. Belytschko, Arbitrary discontinuities in space–time finite elements by level sets and X-FEM, Int. J. Numer. Methods Eng. 61 (2004) 2595–2614.
[7] N. Moes, E. Bechet, M. Tourbier, Imposing dirichlet boundary conditions in the extended finite element method, Int. J. Numer. Methods Eng. 67 (12) (2006) 1641–1669.
[8] C. Comi, S. Mariani, U. Perego, An extended FE strategy for transition from continuum damage to mode I cohesive crack propagation, Int. J. Numer. Anal. Methods Geomech. 31 (2) (2007) 213–238.
[9] C. Comi, S. Mariani, Extended finite element simulation of quasi-brittle fracture in functionally graded materials, Comput. Methods Appl. Mech. Eng. 196 (2007) 4013–4026.
[10] S. Mariani, U. Perego, Extended finite element method for quasi-brittle fracture, Int. J. Numer. Methods Eng. 58 (2003) 103–126.
[11] J. Chessa, T. Belytschko, An extended finite element method for two-phase fluids, J. Appl. Mech. (Trans. ASME) 70 (1) (2003) 10–17.

[12] P. Minev, T. Chen, K. Nandakumar, A finite element technique for multifluid incompressible flow using eulerian grids, J. Comput. Phys. 187 (1) (2003) 255–273.
[13] S. Groß, A. Reusken, An extended pressure finite element space for two-phase incompressible flows with surface tension, J. Comput. Phys. 224 (1) (2007) 40–58.
[14] S. Groß, V. Reichelt, A. Reusken, A finite element based level set method for two-phase incompressible flows, Comput. Vis. Sci. 9 (4) (2006) 239–257.
[15] S. Groß, A. Reusken, Finite element discretization error analysis of a surface tension force in two-phase incompressible flows, IGPM Report 262, RWTH Aachen (2006).
[16] A. Gerstenberger, W.A. Wall, An extended finite element method based approach for large deformation fluid-structure interaction, in: P. Wesseling, E. Oñate, J. Priaux (Eds.), European Conference on Computational Fluid Dynamics, ECCOMAS CFD 2006, 2006.
[17] A. Gerstenberger, W. Wall, An eXtended Finite Element/Mortar Method based approach for fluid-structure interaction, Comput. Methods Appl. Mech. Eng. 197 (2008) 1699–1714.
[18] T. Fries, T. Belytschko, The intrinsic XFEM: a method for arbitrary discontinuities without additional unknowns, Int. J. Numer. Methods Eng. 68 (2006) 1358–1385.
[19] A. Kölke, A. Legay, An enriched space-time finite element method for fluid-structure interaction – part I: presribed structural displacement, in: C.M. Soares (Ed.), Proceedings of the II European conference on Computational Mechanics, Lisbon, Portugal, 2006.
[20] A. Kölke, A. Legay, An enriched space-time finite element method for fluid-structure interaction – part II: thin flexible structures, in: C.M. Soares (Ed.), Proceedings of the II European conference on Computational Mechanics, Lisbon, Portugal, 2006.
[21] A. Zilian, A. Legay, The enriched space-time finite element method (est) for simulation solution of fluid-structure interaction, Int. J. Numer. Methods Eng. 75 (2007) 305–334.
[22] V. Rao, T. Hughes, K. Garikipati, On modelling thermal oxidation of Silicon II: numerical aspects, Int. J. Numer. Methods Eng. 47 (2000) 359–377.
[23] F. Williams, Combustion Theory, second ed., Perseus Books, 1985.
[24] M. Matalon, C. Cui, J. Bechtold, Hydrodynamic theory of premixed flames: effects of stoichiometry, variable transport coefficients and arbitrary reaction orders, J. Fluid Mech. 487 (2003) 179–210.
[25] A.G. Class, B.J. Matkowsky, A.Y. Klimenko, Stability of planar flames as gasdynamic discontinuities, J. Fluid Mech. 491 (2003) 41–63.
[26] D. Nguyen, R. Fedkiw, M. Kang, A boundary condition capturing method for incompressible flame discontinuities, J. Comput. Phys. 172 (28) (2001) 71–98.
[27] F. Gibou, L. Chen, D. Nguyen, S. Banerjee, A level set based sharp interface method for the multiphase incompressible Navier–Stokes equations with phase change, J. Comput. Phys. 222 (2007) 536–555.
[28] Y. Rastigejev, M. Matalon, Numerical simulation of flames as gas-dynamic discontinuities, Combust. Theory Model. 10 (3) (2006) 459–481.
[29] H. Pitsch, L.D. de Lageneste, Large-eddy simulation of premixed turbulent combustion using a level-set appraoch, Proc. Combust. Inst. 29 (2002) 2001–2008.
[30] H. Pitsch, A consistent level set formulation for large-eddy simulation of premixed turbulent combustion, Combust. Flame 143 (2005) 587–598.
[31] W. Kim, S. Menon, Numerical modeling of turbulent premixed flames in the thin-reaction-zones regime, Combust. Sci. Technol. 160 (2000) 119–150.
[32] B. Helenbrook, L. Martinelli, C. Law, A numerical method for solving incompressible flow problems with a surface of discontinuity, J. Comput. Phys. 148 (2) (1999) 366–396.
[33] B. Helenbrook, C. Law, The role of Landau–Darrieus instability in large scale flows, Combust. Flame 117 (1) (1999) 155–169.
[34] K. Pan, W. Shyy, C. Law, An immersed-boundary method for the dynamics of premixed flames, Int. J. Heat Mass Transf. 45 (17) (2002) 3503–3516.
[35] J. Qian, G. Tryggvason, C. Law, A front tracking method for the motion of premixed flames, J. Comput. Phys. 144 (1) (1998) 52–69.
[36] A. Legay, J. Chessa, T. Belytschko, An Eulerian–Lagrangian method for fluid–structure interaction based on level sets, Comput. Methods Appl. Mech. Eng. 195 (17–18) (2006) 2070–2087.
[37] H. Ji, J. Dolbow, On strategies for enforcing interfacial constraints and evaluating jump conditions with the extended finite element method, Int. J. Numer. Methods Eng. 61 (2004) 2508–2535.
[38] J. Douglas Jr., T. Dupont, Interior penalty procedures for elliptic and parabolic Galerkin methods, Lecture Notes in Physics 58 (1976) 207–216.
[39] E. Burman, P. Hansbo, Edge stabilization for galerkin approximations of convection–diffusion–reaction problems, Comput. Methods Appl. Mech. Eng. 193 (2004) 15–16.
[40] E. Burman, A. Ern, Continuous interior penalty hp-finite elements methods for tansport operators, in: A. de Castro, D. Gomez, P. Quintela, P. Salgado (Eds.), Numerical Mathematics and Advanced Applications, Proceedings ENUMATH 2005, Springer, Heidelberg, 2006, pp. 505–511.
[41] I. Babuska, The finite element method with Lagrange multipliers, Numer. Math. 20 (1973) 179–192.
[42] J. Pitkäranta, Boundary subspaces for the finite element method with lagrange multipliers, Numer. Math. 33 (3) (1979) 273–289.
[43] J. Pitkäranta, Local stability conditions for the babuska method of lagrange multipliers, Math. Comput. 35 (152) (1980) 1113–1129.
[44] P. Hansbo, C. Lovadina, I. Perugia, G. Sangalli, A Lagrange multiplier method for the finite element solution of elliptic interface problems using non-matching meshes, Numer. Math. 100 (1) (2005) 91–115.
[45] D.N. Arnold, An interior penalty finite element method with discontinuous elements, SIAM J. Numer. Anal. 19 (4) (1982) 742–760.
[46] E. Marchandise, J. Remacle, A stabilized finite element method using a discontinuous level set approach for solving two phase incompressible flows, J. Comput. Phys. 219 (2) (2006) 780–800.
[47] N. Moes, J. Dolbow, T. Belytschko, A finite element method for crack growth without remeshing, Int. J. Numer. Methods Eng. 46 (1) (1999) 131–150.
[48] M. Braack, E. Burman, V. John, G. Lube, Stabilized finite element methods for the generalized Oseen problem, Comput. Methods Appl. Mech. Eng. 196 (4–6) (2007) 853–866.
[49] T.J.R. Hughes, G. Scovazzi, L.P. Franca, Multiscale and stabilized methods, in: E. Stein, R. de Borst, T.J.R. Hughes (Eds.), Encyclopedia of Computational Mechanics, John Wiley & Sons, Ltd., 2004.
[50] S. Brenner, L. Scott, The Mathematical Theory of Finite Element Methods, Texts in Applied Mathematics, Springer, 2002.
[51] S. Shepel, B. Smith, New finite-element/finite-volume level set formulation for modelling two-phase incompressible flows, J. Comput. Phys. 218 (2) (2006) 479–494.
[52] M. Sussman, P. Smereka, S. Osher, A level set approach for computing solutions to incompressible two-phase flow, J. Comput. Phys. 114 (1) (1994) 146–159.
[53] M. Sussman, E. Fatemi, P. Smereka, S. Osher, Improved level set method for incompressible two-phase flows, Comput. Fluids 27 (5) (1998) 663–680.
[54] L. Landau, E. Lifshitz, Fluid mechanics, Course of Theoretical Physics, Vol. 6, Pergamon, Elmsford, NY, 1959.
[55] T. Poinsot, T. Echekki, M. Mungal, A study of the laminar flame tip and implications for premixed turbulent combustion, Combust. Sci. Technol. 81 (1) (1992) 45–73.